



香港城市大學
City University of Hong Kong

專業 創新 胸懷全球
Professional · Creative
For The World

CityU Scholars

Highly printable, strong, and ductile ordered intermetallic alloy

Zhou, Yinghao; Xiao, Weicheng; Wang, Dawei; Tang, Xu; Shen, Zheling; Li, Weipeng; Zhang, Jun; Zhao, Shijun; Luan, Junhua; An, Zibing; Shi, Rongpei; Yan, Ming; Han, Xiaodong; Liu, C. T.; Zhao, Yilu; Yang, Tao

Published in:

Nature Communications

Published: 01/01/2025

Document Version:

Final Published version, also known as Publisher's PDF, Publisher's Final version or Version of Record

License:

CC BY-NC-ND

Publication record in CityU Scholars:

[Go to record](#)

Published version (DOI):

[10.1038/s41467-025-56355-2](https://doi.org/10.1038/s41467-025-56355-2)

Publication details:

Zhou, Y., Xiao, W., Wang, D., Tang, X., Shen, Z., Li, W., Zhang, J., Zhao, S., Luan, J., An, Z., Shi, R., Yan, M., Han, X., Liu, C. T., Zhao, Y., & Yang, T. (2025). Highly printable, strong, and ductile ordered intermetallic alloy. *Nature Communications*, 16, Article 1036 . <https://doi.org/10.1038/s41467-025-56355-2>

Citing this paper

Please note that where the full-text provided on CityU Scholars is the Post-print version (also known as Accepted Author Manuscript, Peer-reviewed or Author Final version), it may differ from the Final Published version. When citing, ensure that you check and use the publisher's definitive version for pagination and other details.

General rights

Copyright for the publications made accessible via the CityU Scholars portal is retained by the author(s) and/or other copyright owners and it is a condition of accessing these publications that users recognise and abide by the legal requirements associated with these rights. Users may not further distribute the material or use it for any profit-making activity or commercial gain.

Publisher permission

Permission for previously published items are in accordance with publisher's copyright policies sourced from the SHERPA RoMEO database. Links to full text versions (either Published or Post-print) are only available if corresponding publishers allow open access.

Take down policy

Contact lbscholars@cityu.edu.hk if you believe that this document breaches copyright and provide us with details. We will remove access to the work immediately and investigate your claim.

Highly printable, strong, and ductile ordered intermetallic alloy

Received: 20 July 2024

Accepted: 13 January 2025

Published online: 25 January 2025

 Check for updates

Yinghao Zhou^{1,2}, Weicheng Xiao¹, Dawei Wang³, Xu Tang⁴, Zheling Shen⁵, Weipeng Li³, Jun Zhang², Shijun Zhao², Junhua Luan², Zibing An⁶, Rongpei Shi⁴, Ming Yan³, Xiaodong Han⁶, C. T. Liu^{1,7}, Yilu Zhao⁴ ✉ & Tao Yang^{1,2,7} ✉

Ordered intermetallic alloys are renowned for their impressive mechanical, chemical, and physical properties, making them appealing for various fields. However, practical applications of them have long been severely hindered due to their severe brittleness and poor fabricability. It is difficult to fabricate such materials into components with complex geometries through traditional subtractive manufacturing methods. Here, we proposed a strategy to solve these long-standing issues through the additive manufacturing of chemically complex intermetallic alloy (CCIMA) based on laser powder bed fusion (LPBF). The developed CCIMA exhibits good printability, enabling a crack-free microstructure with a low porosity of 0.005%. More importantly, a good combination of high tensile strength (~1.6 GPa) and large uniform elongation (~35%) can be achieved, which has not been reported in the existing additive-manufactured alloys. Such properties are attributed to the structural and chemical features of highly ordered superlattice grain decorated with disordered interfacial nanolayer, as well as dynamic evolutions and interactions of multiple dislocation substructures. These findings could provide references for developing high-performance intermetallic alloys and accelerating their practical applications.

Intermetallic alloys with ordered structures constitute a distinct category of materials that bridge the gap between ceramics and metallic alloys and provide copious advantages for advanced structural applications across various contemporary industries, such as aerospace, energy, automotive, etc.^{1,2}. Unlike disordered alloys, the long-range ordering could generate strong chemical bonding between atoms, low atomic mobility, and unusual dislocation behaviors^{3,4}. These features potentially endow intermetallic alloys with many attractive properties,

such as anomalous yielding behavior, high work-hardening capability, and good chemical resistance, etc.^{3,4}. However, despite these promising advantages, their large-scale applications are still significantly constrained due to the serious contradiction between strength and ductility, especially at ambient temperature⁵. For example, most bulk intermetallic alloys with high tensile strength over 1 GPa generally suffer from limited ductility, making them impossible to be reliably used in engineering fields⁶. Another critical bottleneck lies in their

¹Department of Materials Science and Engineering, College of Engineering, City University of Hong Kong, Hong Kong, China. ²Department of Mechanical Engineering, College of Engineering, City University of Hong Kong, Hong Kong, China. ³Department of Materials Science and Engineering, Shenzhen Key Laboratory for Additive Manufacturing of High-performance Materials, Southern University of Science and Technology, Shenzhen, China. ⁴School of Materials Science and Engineering, Harbin Institute of Technology (Shenzhen), Shenzhen, China. ⁵Shenyang National Laboratory for Materials Science, Institute of Metal Research, Chinese Academy of Sciences, Shenyang, China. ⁶Department of Materials Science and Engineering, Southern University of Science and Technology, Shenzhen, China. ⁷Hong Kong Branch of National Precious Metals Material Engineering Research Centre (NPMM), City University of Hong Kong, Hong Kong, China. ✉ e-mail: zhaoyilu@hit.edu.cn; taoyang6-c@my.cityu.edu.hk

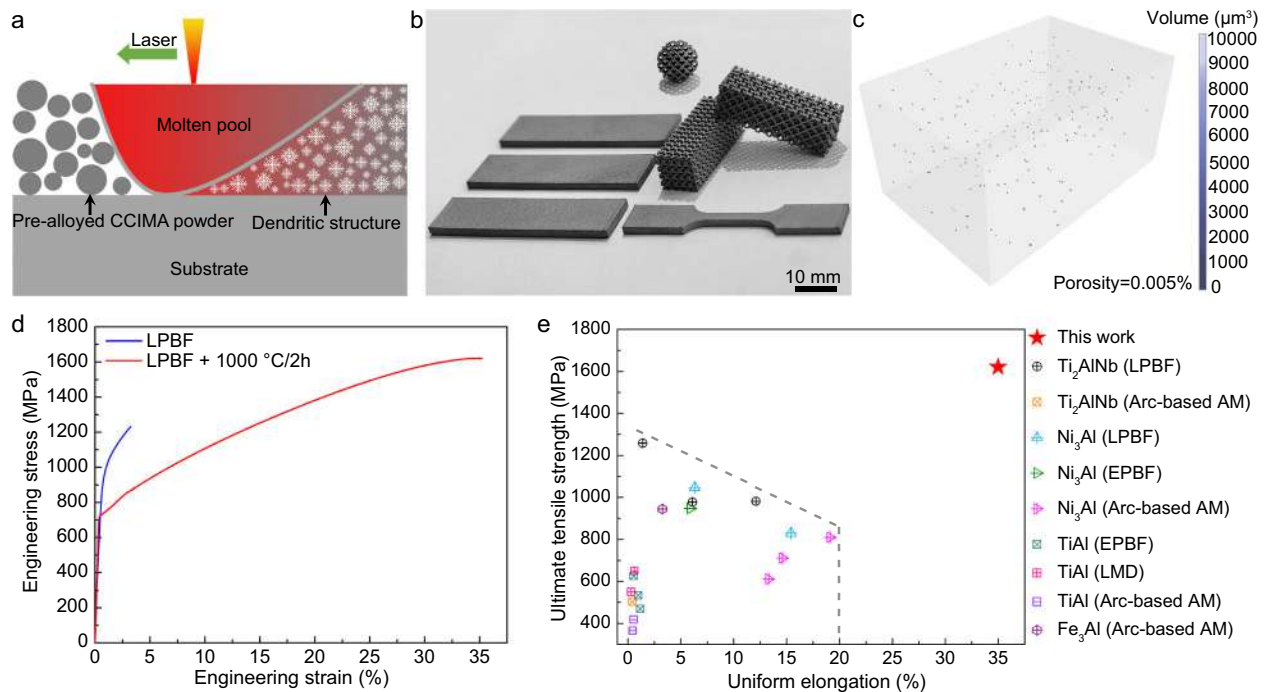


Fig. 1 | Printability and tensile properties of the CCIMA. **a** Schematic diagram showing the manufacturing of CCIMA by the LPBF technique, the red color in molten pool representing the high-temperature region. **b** The solid samples and hollow samples with intricate lattice structures illustrating the good fabricability of the CCIMA. **c** The pore defect distribution of the as-printed CCIMA measured by the micro-CT, the color bar corresponding to the volume of the pores. **d** Engineering

tensile stress-strain curves of the as-printed and thermal-stabilized CCIMA samples. **e** Comparison of ultimate tensile strength versus uniform elongation of the present CCIMA with conventional intermetallic alloys fabricated by various AM techniques, including LPBF, arc-based AM, electron beam powder bed fusion (EPBF), laser metal deposition (LMD), the grey dash line representing the performance boundary between conventional intermetallic alloys and CCIMA.

poor fabricability¹. Usually, to achieve decent properties of the intermetallic alloys, complex processing methods involving vacuum melting and casting, repetitive rolling and heating have to be applied, which is not only time-consuming but also very costly. In particular, fabricating intermetallic components with intricate geometries and structures also poses significant challenges and difficulties when relying on these conventional subtractive manufacturing techniques.

Remarkably, additive manufacturing (AM) or three-dimensional (3D) printing can flexibly design and fabricate components with customized complicated structures via a layer-by-layer way^{7,8}, offering a promising strategy for the near-net-shape fabrication of intermetallic alloys. Despite many years of efforts, the printability and mechanical properties of intermetallic alloys have so far remained unsatisfactory, mainly stemming from the severe cracking caused by the high cooling rate of most AM processes^{9–12}. For example, the Ni₃Al-based IC-221M alloy fabricated by LPBF exhibited unavoidable solidification cracking, which is hard to be eliminated only through optimizing the printing parameters⁹. Hot isostatic pressing can potentially solve this problem by healing the cracks, which, however, inevitably requires quite complicated equipment with high costs and low efficiency. Meanwhile, regarding the material innovation, most existing studies are focused on the conventional intermetallic alloys with simple chemistries, such as the Ni₃Al^{9,10}, NiAl¹¹, TiAl¹², etc., making it very challenging to break through this long-standing issue.

To this end, in our present study, distinguishing from the conventional wisdom, we designed a L₂-type CCIMA based on a multi-element Ni-Co-Si-Ti-Al-B system, which demonstrates good printability during the LPBF, maintaining crack-free with a low porosity. With just a single-step thermal stabilization treatment, the microstructural features composed of ordered grain and disordered nanolayer at grain boundary can be achieved. Consequently, the developed CCIMA enables superb strength-ductility synergy at ambient temperature,

which has not been observed in the additively manufactured conventional intermetallic alloys until now.

Results and Discussion

We first applied the LPBF to melt and deposit the pre-alloyed CCIMA (Ni_{58.48}Co_{18.9}Si_{11.6}Ti_{6.6}Al_{4.4}B_{0.02}, in atomic percentage (at. %)) powders. The schematic diagram of LPBF CCIMA is illustrated in Fig. 1a. Unlike most conventional intermetallic alloys with poor printability, the present CCIMA can be well manufactured using the LPBF technique. Besides the solid samples, the hollow samples with intricate lattice structures can also be precisely manufactured directly from the spherical pre-alloyed CCIMA powder (Fig. 1b). Nearly fully dense samples were well obtained when the laser scanning speeds varied from 600 to 1000 mm/s (Supplementary Fig. 1). Figure 1c further exhibits the micro-focus computed tomography (micro-CT) result of the sample fabricated at a laser scanning speed of 900 mm/s. The statistical distribution of pore size was provided in the Supplementary Fig. 2, showing an average pore diameter of 22.0 μm. Only a few pore defects with a low porosity of 0.005% were detected in the as-printed CCIMA. In particular, there are no micro-cracks as revealed by the micro-CT or optical microscopy results, which is different from conventional intermetallic alloys that usually suffer from serious cracking during the LPBF^{9–12}. The mechanism of pore formation during LPBF conditions was further elucidated using multi-physics simulation (Supplementary Note 1). The powder bed model and parameters used in the computational fluid dynamics (CFD) simulations are presented in Supplementary Fig. 3 and Supplementary Table 1, respectively. As shown in the Supplementary Fig. 4a, b, noticeable pore defects are present within the melt tracks at a laser scanning speed of 500 mm/s. However, these defects are reduced when the laser scanning speed is increased to 900 mm/s, consistent with the experimental observations (Supplementary Fig. 1). The complete pore formation process in LPBF

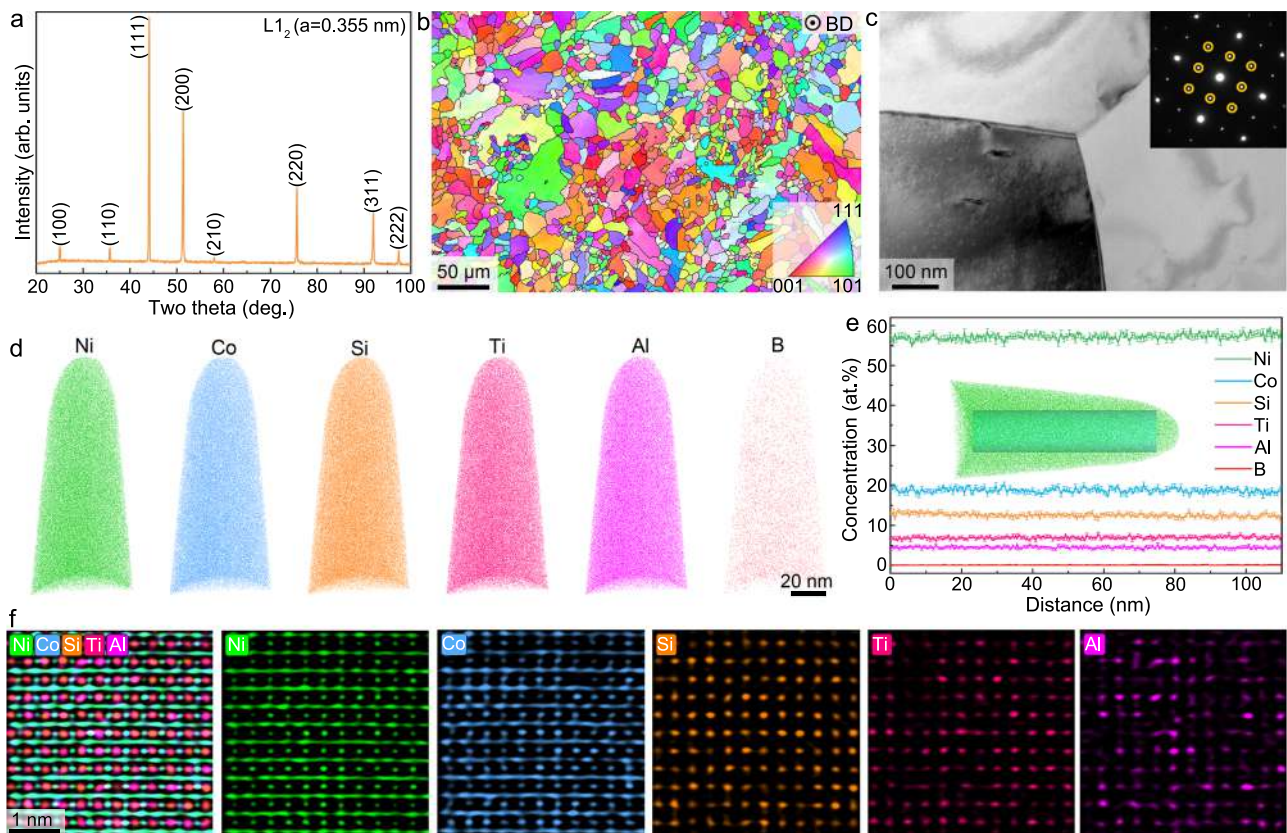


Fig. 2 | Microstructural features of the thermal-stabilized CCIMA from microscopic to atomic scales. **a** XRD spectrum illustrating an ordered $L1_2$ -type crystal structure. **b** EBSD-IPF map showing the fine grain morphology perpendicular to the building direction (BD), the color representing the crystal orientation. **c** TEM bright-field image showing the homogeneous grain structure, the inset of **(c)** showing the diffraction pattern of the grain along $[001]$ crystal zone axis, the superlattice diffraction spots highlighted by the yellow circles in the SAED pattern

illustrating a highly ordered $L1_2$ structure of the grain interior. **d** 3D-APT results showing the homogeneous elements distribution within the grain interior. **e** One-dimensional concentration profile showing the element distributions across the 3D-APT tip, the error bar representing the standard deviation of atomic fraction of each element. **f** Atomic EDS maps taken from the ordered grain interior along the $[001]$ crystal zone axis, showing the spatial occupations of each element.

CCIMA is detailed in Supplementary Fig. 4c–g. The reduction in pore defects at higher laser scanning speed can be attributed to the enhanced stability of keyhole and melt flow, as demonstrated in the Supplementary movies. Besides the low porosity, we also printed some standard features such as holes and rods with different sizes to illustrate the dimensional accuracy of the as-printed CCIMA. As presented in Supplementary Fig. 5 and Supplementary Tables 2 and 3, the as-printed holes and rods show high dimensional accuracy with very small experimental errors, indicating a high printability of the CCIMA. Based on the simulation results and experimental validations, the processing window (laser power and scanning speed) that eliminates pore formation process was determined, thereby improving the geometric quality of melt tracks.

Then, the as-printed CCIMAs are subjected to a single-step thermal stabilization treatment ($1000\text{ }^\circ\text{C}/2\text{ h}$). The engineering tensile stress-strain curves of both as-printed and thermal-stabilized CCIMAs are provided in Fig. 1d. The thermal-stabilized CCIMA exhibits a high tensile strength, reaching up to $1620 \pm 30\text{ MPa}$, and concurrently preserves a large uniform elongation of $35 \pm 3\%$ (Fig. 1d). The fracture surface was first characterized by scanning electron microscopy (SEM). No grain-boundary dissociation can be identified on the overall fracture surface. (Supplementary Fig. 6a). Meanwhile, numerous microdimples are spread across the fracture surface (Supplementary Fig. 6b), indicating an intrinsic ductile feature of this alloy. The strength-ductility synergy of our CCIMA is superior to these conventional intermetallic alloys fabricated by various AM methods (including Ni_3Al ^{9,13,14}, Fe_3Al ¹⁵, TiAl ^{16–18}, and Ti_2AlNb ¹⁹) (Fig. 1e), as well as other types

of state-of-the-art alloys, such as Ni-based superalloys^{20–22}, steels²³, and Ti alloys^{24–26}, and high-entropy alloys (face-centered cubic (FCC) HEAs^{27,28}, eutectic HEAs^{29,30}, $L1_2$ -hardened HEAs^{31,32}, ceramic-hardened HEAs^{33–35}) (Supplementary Fig. 7).

To unveil the intrinsic origins of such a high strength-ductility combination of the LPBF CCIMA, we carefully examined the microstructural features ranging from microscopic to atomic scales. As illustrated in Fig. 2a, the X-ray diffraction (XRD) spectrum with obvious superlattice peaks confirms the formation of a highly ordered $L1_2$ -type crystal structure of the thermal-stabilized CCIMA without detecting any other detrimental phases. The electron backscatter diffraction (EBSD) inverse pole figure (IPF) map in Fig. 2b shows the random grain distribution with a maximum texture index of 2.56, as revealed by the pole figure in Supplementary Fig. 8a. The grain size distribution is shown in Supplementary Fig. 8b, revealing an average grain size of $17.7\text{ }\mu\text{m}$. The back scattered electron (BSE) image together with the energy dispersive spectroscopy (EDS) maps demonstrate fully equiaxed grains with homogeneous elemental distributions (Supplementary Fig. 8c–h). The overall chemical composition of the thermal-stabilized CCIMA measured by SEM-EDS is $\text{Ni}_{58.1}\text{Co}_{19.5}\text{Si}_{11.5}\text{Ti}_{6.6}\text{Al}_{4.3}$ (at. %), showing a very small chemical change compared with the pre-alloyed powder. The transmission electron microscopy-bright field (TEM-BF) image (Fig. 2c) further illustrates that the dendritic microstructure consisting of brittle G phase³⁶ existed in the as-printed CCIMA was effectively eliminated after the simple thermal treatment (Supplementary Note 2, Supplementary Fig. 9 and Fig. 10). The obvious superlattice spots in the selected area electron diffraction (SAED)

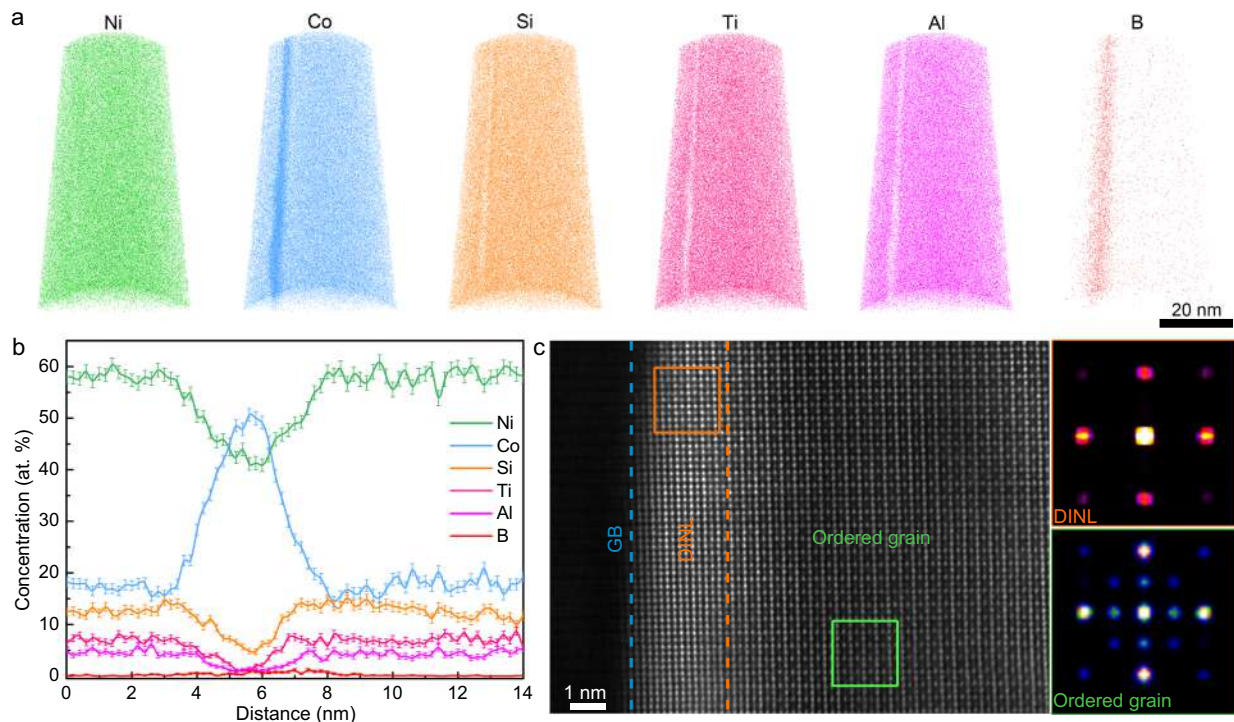


Fig. 3 | Chemical and atomic structures of the DINL and ordered grain interior. **a** 3D-APT maps showing the distribution of each element near the grain boundary. Elements Co and B co-segregated to the DINL, while Ni, Si, Ti, and Al depleted accordingly. **b** One-dimensional compositional profile revealing the elemental distributions across the grain interior and DINL, the error bar representing the

standard deviation of atomic fraction of each element. **c** Atomic-resolution STEM-HAADF image illustrating the atomic structures of the DINL and grain interior, the corresponding FFT images (insets in c) showing the disordered structure of the DINL and ordered structure of grain interior.

pattern (inset in Fig. 2c) indicate a highly ordered structure of the grains. The elements (Ni, Co, Si, Ti, Al, B) inside the grain interior were quantitatively analyzed using three-dimensional atom probe tomography (3D-APT), revealing homogeneous compositional distributions without undesired elemental clustering or precipitation in an atomic scale (Fig. 2d, e). The detailed composition for each element obtained by the 3D-APT is provided in Supplementary Table 4. We further conducted the aberration corrected-scanning TEM (AC-STEM) under the high-angle annular dark-field (HAADF) image mode together with atomic-resolution EDS to probe the spatial site-occupancy behavior of each element within the ordered L_2 structure (Fig. 2f). Atoms Ni and Co mainly occupy the faced centers (A-type sublattice) of the L_2 unit cell, while the vertices (B-type sublattice) are occupied by the atoms Si, Ti, and Al. Thus, based on these, the ordered L_2 structure here can be finally identified as the $(\text{Ni, Co})_3(\text{Si, Ti, Al})$ -type chemically complex ordered superlattice structure.

The grain boundaries of intermetallic alloys usually suffer from serious embrittlement during tensile deformation, leading to easy cracking and intergranular fractures with poor ductility³⁷. An interesting but critical question is what is the intrinsic reason for the large uniform elongation in the present CCIMA especially under such a high-strength level? For this purpose, we carefully examined the structural and compositional features along the grain boundaries. As illustrated in the 3D-APT results (Fig. 3a), a distinct nanolayer can be clearly identified near the grain boundary, which is strongly rich in elements Co and B, but depleted in elements Ni, Si, Ti, and Al. The one-dimensional compositional profile provided in Fig. 3b quantitatively gives the compositional variations across this nanolayer. We found that the concentration of elements Co and B gradually increased from the grain interior to the grain boundary, while other elements showed the opposite trend. The maximum concentration of the element Co inside the nanolayer can reach -50.64 ± 1.23 at. %, which is much higher

than that in the grain interior (-18.95 ± 2.04 at. %). We also observed a pronounced B segregation (up to 0.85 ± 0.22 at. %) in the nanolayer, much higher than that inside the grain (around 0.02 ± 0.01 at. %). The atomic structure of this nanolayer was further characterized by the AC-STEM technique. As presented in Fig. 3c, a distinctive interfacial nanolayer can be observed near the grain boundary, which was identified as a disordered FCC solid-solution structure (γ phase) based on the corresponding Fast Fourier Transform (FFT) image (Fig. 3c). Meanwhile, this disordered interfacial nanolayer (DINL) is highly coherent with the adjacent ordered L_2 grain. The thickness of DINL is about 5 nm based on the 3D-APT (Fig. 3b) and atomic-resolution STEM-HAADF images (Fig. 3c). The volume fraction of the DINL can be estimated by the equation of $f_{\text{DINL}} = 1 - (1 - t/d)^3$, where t is the thickness of DINL, d is the average grain size ($17.7 \mu\text{m}$)³⁸. Thus, the volume fraction of DINL is calculated to be 0.08%. These distinctive structural and chemical characteristics along the grain boundaries, i.e., the DINL and co-segregation of B and Co atoms, are vital for overcoming the strength-ductility trade-off that is typically encountered in traditional intermetallic alloys.

To reveal the crucial effect of the DINL in eliminating the intergranular embrittlement, geometrically-necessary dislocation (GND) distributions under different deformation strains were measured using the EBSD method. Compared with the highly ordered grains, the DINLs without anti-phase boundary (APB) barriers are more prone to dislocation multiplication and pile up. Thus, with the increase of stress and strain, apparent aggregations of GNDs were formed in the vicinity of grain boundaries (Fig. 4a–c), indicating that grain boundaries bore much higher stress than the grain interior. However, cracks were not nucleated and propagated along the grain boundaries, leading to a transgranular fracture behavior (inset in Fig. 1d). This means that the thermal-stabilized CCIMA possesses strong but ductile interfaces between the ordered grains, which is different from traditional

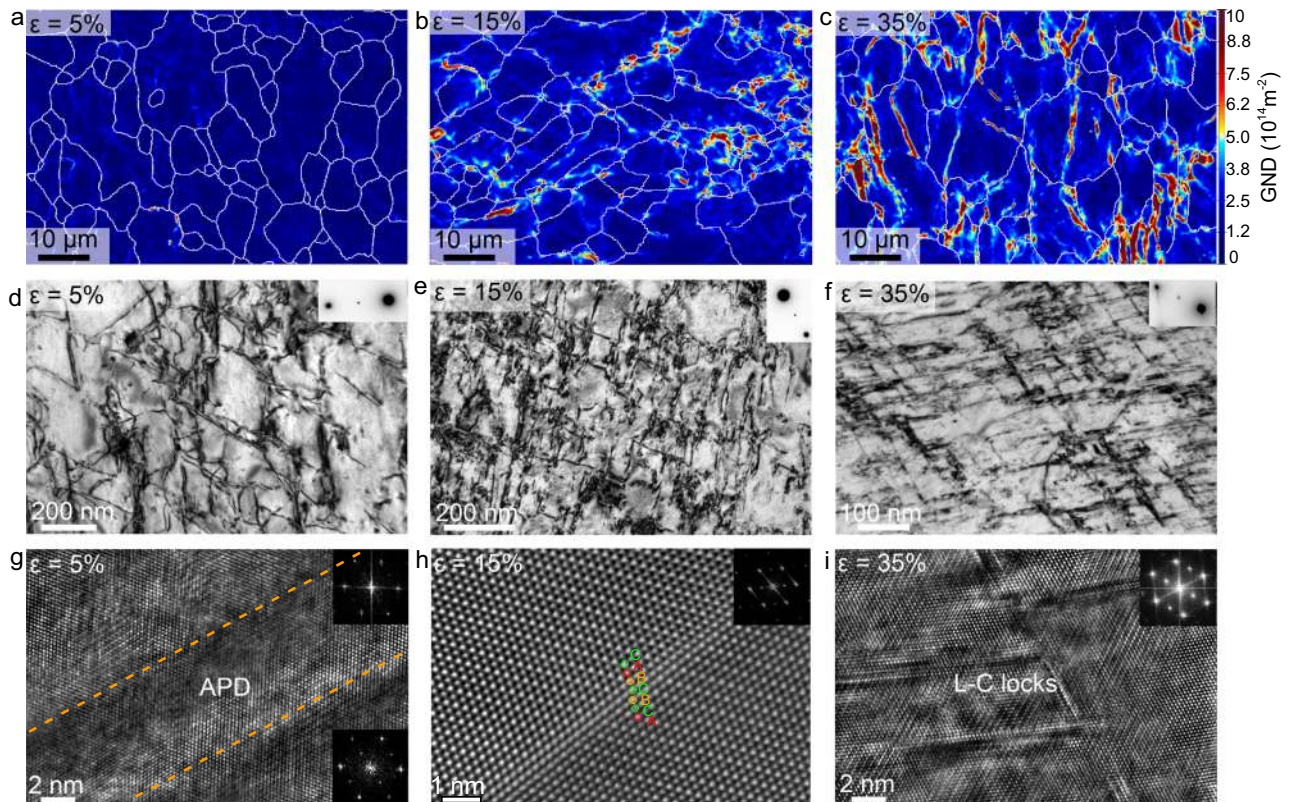


Fig. 4 | Deformation mechanism of the CCIMA at different tensile strains. **a–c** GND distribution maps revealing the varied stress concentrations near the grain boundaries with the increase of deformation strains from 5% to 35%, the white line representing grain boundary, while the color bar representing GND density. **d–f** TEM bright field images taken along the (200) two-beam condition showing the

morphologies of deformation substructures of the CCIMA at different strains. **g, i** High-resolution TEM and corresponding FFT images (insets) revealing the changes in the types of deformation substructures from APB-coupled superlattice dislocations (5%) to intersected SFs (35%). **h** Atomic-resolution STEM-HAADF image illustrating the existence of SISF at a strain of 15%.

intermetallic alloys that usually suffer from serious grain-boundary fractures³⁹. The underlying mechanism for the ductilization by disordering is attributed to the degradation of ordering energy and enhancement of the atomic relaxation⁴⁰. Dislocation slip is therefore easy to be activated in the DINL compared with the highly ordered grain interior. To support this viewpoint, the dislocation behavior near the grain-boundary region of the deformed sample with a strain of 5% was further checked using STEM. As shown in Supplementary Fig. 11, dislocations accumulated at the DINL and piled up against grain boundaries (GBs), indicating that the relatively soft DINL can sustain larger plastic strain prior to the hard $L1_2$ region, which decreased the possibility of forming cracks and finally contributed to the high ductility. The formation of this unique DINL can be attributed to the segregation of element Co (Fig. 3a), which is a strong FCC stabilizer. Extra Co atoms in the DINL tend to substitute the Ni site and degrade the ordering energy, stabilizing the disordered FCC phase⁴⁰. Meanwhile, the Co segregation generates slightly covalent Ni-Co bonds and hence weakens the covalency of Ni-Al bonds^{41,42}. Thus, the diffusion of Al via the vacancy diffusion mechanism becomes easier, which promotes the anti-site occupation behavior (A-site atoms enter into B sites) and then destroys the long-range ordering of the $L1_2$ phase^{41,42}.

Besides the DINL, the segregation of B atoms in the grain boundary is also an essential factor for toughening the CCIMA. It is reported that element B is less electronegative compared to base alloy⁴³. Thus, B atoms prefer to share electrons with the metal atoms (i.e., formation of homopolar bonds) rather than capture electrons from them, which enhances the bonding between atoms⁴³. Thus, the segregation of B atoms can improve the cohesive strength of the grain boundaries in present CCIMA and reduce the tendency of brittle

intergranular fracture. Meanwhile, the enrichment of Co near the grain boundaries may further enhance the electronic interaction with B atoms, increasing the ductilization effect of B atoms⁴³. Therefore, under high-stress concentrations, the strong grain boundaries can respond through the activation of dislocation sources in neighboring grains, which relaxes stress concentrations caused by the dislocation accumulation, leading to the slip transfer across grain boundaries and eventually spread across the grains⁴⁴. In contrast, weak grain boundaries are usually accompanied by the formation and propagation of cracks to relieve stress concentration⁴⁴.

Under the guarantee of strong grain boundaries, plastic deformation within the ordered grain interior was realized. The true stress-strain curve in the Supplementary Fig. 12a reveals that the true stress can be hardened from 730 to 2190 MPa after yielding, indicating a high work hardening rate (WHR), which derives from the special dislocation behaviors within the multi-element $L1_2$ -type superlattice structure. The curves of WHR and work hardening exponent (WHE) as a function of true strain are plotted in Supplementary Fig. 12b, showing three distinct deformation stages. The maximum WHR and WHE are achieved in stage II, showing an anomalously high value of 5.1 GPa and 0.6, respectively. These surpass most metallic materials, including HEAs^{45,46}, Ni-based superalloys⁴⁷, and steels^{48,49}. The high WHR and WHE indicate that the thermal-stabilized CCIMA can sustain superb work-hardening capacity and uniform plastic deformation capability even at a high engineering strain of up to 35%. The underlying reasons for the high WHR and WHE are attributed to the rapid increase in dislocation density. During the plastic deformation, the mean free path for the movement of superlattice dislocations is much smaller in ordered intermetallics than that in disordered

alloys⁵⁰. Therefore, the superlattice dislocations have a high probability of being blocked and stored in the ordered crystal structure dynamically and steadily. The increment of superlattice dislocation density of present CCIMA under different deformation strains can be calculated using the modified Williamson-Hall method (Supplementary Note 3). As presented in Supplementary Fig. 12c, the XRD peaks show obvious broadening with the increase of deformation strains from 5% to 35%, indicating a rapid increase in dislocation density from 0.16 to $5.34 \times 10^{15} \text{ m}^{-2}$ (Supplementary Fig. 12d). Consequently, the rapid accumulation of dislocation density plays a substantial role in maintaining effective work hardening, contributing to the achievement of high uniform elongation.

To further uncover the intrinsic origins of the ultrahigh WHR, detailed deformation mechanisms under different deformation stages were studied using TEM coupled with density functional theory (DFT) simulations. At a strain of 5%, the superlattice dislocations are distributed uniformly along the {111} close-packed planes and exhibit slight entanglement (Fig. 4d). The weak beam dark field image under the *g*-3*g* condition further confirms that each superlattice dislocation was split into two pairs (Supplementary Fig. 13a). During the slide of superlattice dislocation, the leading superlattice dislocation destroyed the ordered arrangement of atoms on the slip plane, while the slip of following trailing superlattice dislocation restored its ordering. Thus, a disordered region was generated between the superlattice dislocation pairs, leading to the formation of antiphase domain (APD), as proven by the high-resolution TEM and corresponding FFT images (Fig. 4g). During deformation, the APB-coupled superlattice dislocations occurred a cubic cross slip from the primary pyramidal (111) plane to the non-slide cubic (100) plane and were locked on it (Supplementary Fig. 13). This configuration, also called the Kear-Wilsdorf (K-W) lock, is effectively sessile and poses a strong pinning effect on the further movement of dislocations, leading to an anomalously high WHR⁵¹. Besides the superlattice dislocation behavior in the grain interior, the GNDs accumulated near the grain boundary also contributed to the work hardening capability. As shown in Supplementary Fig. 11, dislocations accumulated at the DINL and piled up against GBs, indicating that the relatively soft DINL can sustain larger plastic strain prior to the hard LL₂ region. To coordinate this deformation inhomogeneity, GNDs usually generated in the soft DINL and piled up against GBs, which can act as obstacles to the dislocation motion and lead to generation of back stress, eventually contributing to the work hardening of the CCIMA^{52–54}.

With the increase of deformation strain to 15%, the interactions between superlattice dislocations became more prominent, leading to apparent entanglements of superlattice dislocations and giving rise to extra contribution to work hardening (Fig. 4e). Once the applied stress exceeded the critical resolved shear stress for activating the superlattice stacking fault (SSF), SSF shearing will occur in this condition. Meanwhile, the atomic-resolution STEM-HAADF image in Fig. 4h confirms the stacking sequence of ABCBCABC, proving the formation of SISF. Subsequently, in stage III, the plastic deformation was dominated by high-density SISF networks, as revealed by the TEM image (Fig. 4f) and the elongated diffraction spots (inset of Fig. 4f). High-resolution TEM image also proves that these stacking faults were intersected with each other to form the Lomer-Cottrell (L-C) locks (Fig. 4i). Both the K-W locks and L-C locks effectively impeded the movement of dislocations, contributing to the pronounced work hardening response.

The above-mentioned deformation modes are mainly related to the planar fault energies of APB and SISF on the {111} slip planes. The APB-type dissociation behavior will be favored if the following inequation is satisfied⁵⁵:

$$\ln\left(\frac{8\pi\gamma_{SISF}^{(111)}}{aC_{44}}\right) > 2\ln\left(\frac{4\pi\gamma_{APB}^{(111)}}{aC_{44}}\right) + 1 \quad (1)$$

where $\gamma_{APB}^{(111)}$ and $\gamma_{SISF}^{(111)}$ are the fault energies of APB and SISF on the (111) plane, respectively, and the terms of *a* and *C*₄₄ are the lattice constant and elastic constant of the CCIMA. Based on the DFT calculations, the values of $\gamma_{APB}^{(111)}$, $\gamma_{SISF}^{(111)}$, and *C*₄₄ are calculated to be 301 mJ/m², 200 mJ/m², and 130.0 GPa, respectively (Supplementary Fig. 14a and b). The DFT calculation method was provided in Supplementary Note 4. Drawing from inequation (1) and the derived parameters, the CCIMA meets the energy threshold for APB-type dissociation (Supplementary Fig. 14c). The data of Ni₃Al, Co₃(Ti,W), Co₃(Ti,Ta) Co₃Ti, are from the reference⁵⁶, the data of Co₃(Al,W), and Ir₃Nb are from the reference⁵⁷, while the data of Fe₃Ge is from the reference⁵⁸. This suggests that the plastic deformation of the CCIMA is predominantly governed by the shearing through APB-coupled dislocations, which is consistent with the experimental results of Fig. 4d. With the increase of deformation strain, the main deformation mechanism gradually changes from APB to SISF dissociation, due to the rapid increase in flow stress.

In summary, we successfully developed a CCIMA via the LPBF additive manufacturing. Unlike the conventional intermetallic alloys with poor printability, the present CCIMA is highly printable and can be well manufactured by the LPBF method. Only by the simple thermal treatment, we achieved microstructures consisting of LL₂-type ordered grains whose boundaries are decorated with disordered nanoscale FCC interfaces co-segregated with elements B and Co. Benefiting from such a special design, a high tensile strength accompanied by large ductility and superb work-hardening capability can be achieved simultaneously, which are unmatched by conventional additive manufactured alloys hitherto reported. It is expected that mechanistic insights taken into the ductilization and strengthening behavior could also be applied to solve the poor fabricability and brittleness of other metallic materials. A broad range of advanced industries would also substantially benefit from such a special design.

Methods

Materials

Pre-alloyed CCIMA powder with a composition of Ni_{58.48}Co_{18.9}Si_{11.6}Ti_{6.6}Al_{4.4}B_{0.02} (at. %) was fabricated using the electrode induction melting gas atomization (EIGA). The powder composition is measured by the inductively coupled plasma-optical emission spectrometry (ICP-OES). Most of the powder particles exhibit a nearly spherical shape (Supplementary Fig. 15a). The particle size was determined by the Mastersizer 3000 laser particle size analyzer, which ranged from 24.2 to 58.2 μm with a mean diameter D₅₀ = 37.6 μm (Supplementary Fig. 15b).

Materials fabrication

The CCIMA samples were manufactured using a commercial SLM®125HL LPBF machine equipped with an IPG fiber laser with a maximum power of 400 W and a laser beam diameter of 64 μm. The LPBF process was conducted in an argon-protective atmosphere with an oxygen content below 400 ppm. The 316 L stainless steel used as the printing substrate was heated up to 200 °C to reduce the residual stress during printing. To investigate the effects of scanning speed on the forming ability of the as-printed CCIMA, the scanning speeds varied from 500 to 1000 mm/s with a permanent increment of 100 mm/s. The layer thickness of 0.03 mm, hatch distance of 0.12 mm, and a laser-beam rotation of 67° for the consecutive layers were fixed for all the samples. The tensile samples were directly printed using the optimized laser power of 200 W, and scanning speed of 900 mm/s. Flat dog-bone-shaped tensile samples with a gauge length of 12.5 mm and a cross-section dimension of $-3.2 \times 3 \text{ mm}^2$ were directly fabricated by the LPBF. The as-printed samples were cut off from the 316 L stainless steel substrate using the wire electrical discharge machining. Thermal stabilization treatment was conducted at 1000 °C for 2 h followed by air cooling to eliminate the non-equilibrium brittle phase and residual stress.

Characterization

The internal defects of the as-printed CCIMA fabricated under different LPBF parameters were first observed using the optical microscopy for preliminary process optimization. The micro-CT experiment was further conducted to determine the porosity of the as-printed CCIMA using the Diondo D2 machine with the W radiation at 30 μ A and 210 kV. The sample used for the micro-CT test with a dimension of $3.0 \times 2.0 \times 1.5 \text{ mm}^3$ was rotated from 0° to 360° with a step size of 0.2° . A flat silicon detector was used to collect the 2D projection images with a scan resolution of 2 μ m.

The phase constitutions, contents, and dislocation densities under different deformation strains were studied using XRD with Cu K α radiation (Rigaku SmartLab) operated at 45 kV and 200 mA, step size of 0.02° , scanning speed of 1 $^\circ/\text{min}$. The phase constitutions and contents of the pre-alloyed powder, as-printed, and thermal-stabilized CCIMA were first determined based on the whole pattern fitting method. The dislocation densities multiplication of the thermal-stabilized CCIMA under different deformation strains were calculated based on the modified Williamson-Hall method⁵⁹. Detailed calculations for the dislocation density were provided in Supplementary Note 3. Samples used for the XRD test were first mechanically polished followed by electrolytic polishing in a mixed solution of $\text{HNO}_3:\text{C}_2\text{H}_6\text{O} = 1:4$ for 20 s with a direct voltage of 20 V at -40°C .

The microstructure of the as-printed sample was characterized by SEM (FEI, Scios, 20 kV, 3 nA) in the BSE mode. EBSD maps were acquired using an EDAX Velocity camera equipped on a FEI Scios microscope at an accelerating voltage of 20 kV and current of 13 nA. The EBSD-IPF mapping is obtained by testing the plane perpendicular to the building direction. Samples for the SEM and EBSD experiments were first mechanically polished with diamond suspension, and then polished with the SiO_2 suspension by the VibroMet[®]2 Vibratory Polisher to provide a stress-free surface. Microstructural features, phase compositions, crystal structures, and deformation substructure were characterized using TEM (JEOL 2100 F and Talos F200) coupled with EDS and SAED. AC-STEM (FEI Titan Themis G2, operated at 300 kV) was further adopted to determine the atomic occupancy of the L1_2 matrix, and the structural feature near the grain boundary in an atomic scale. The samples for TEM tests were first mechanically polished to around 30 μ m using SiC grinding paper, and then punched into 3-mm-diameter discs. A precision ion polishing system (PIPS II, Model 695, Gatan) was further applied to mill these discs to a thickness of electron transparency.

Three-dimensional elemental distribution at the atomic scale was revealed using a local electrode APT (CAMECA LEAP 5000 XR). Needle-shaped samples were annularly milled in a focused ion beam/scanning electron microscope (FIB/SEM, FEI Scios). The 3D-APT experiment was conducted in a voltage mode at 70 K, at a pulse fraction of 20%, a pulse repetition rate of 200 kHz, and an evaporation detection rate of 0.2% atom per pulse. Corresponding data were analyzed using AP Suite 6.1 workstations for creating the 3D reconstructions.

Tensile tests were performed on a Material Testing System (MTS) machine at room temperature with a constant strain rate of $1 \times 10^{-3} \text{ s}^{-1}$. Before tensile tests, the samples were ground to 3000-grit finish using SiC grinding paper. The tensile strain was measured by a clip-on axial extensometer. At least four specimens were tested perpendicular to the building direction to guarantee the data reproducibility. After the tensile test, the fracture surface was observed using SEM in the secondary electron mode (10 kV, 0.4 nA). To reveal the underlying deformation mechanisms, samples deformed at different strains were characterized in detail by collaboratively using XRD, EBSD, and TEM.

Data availability

All the data supporting the results and findings of this study are provided in the paper and the Supplementary Materials. Source data are provided with this paper⁶⁰. Source data are provided with this paper.

References

1. Liu, C., Stringer, J., Mundy, J., Horton, L. & Angelini, P. Ordered intermetallic alloys: An assessment. *Intermetallics* **5**, 579–596 (1997).
2. Jozwik, P., Polkowski, W. & Bojar, Z. Applications of Ni_3Al based intermetallic alloys—current stage and potential perceptivities. *Materials* **8**, 2537–2568 (2015).
3. Pope, D. High temperature ordered intermetallic alloys. *MRS Online Proc. Libr.* **81**, 3–11 (1986).
4. Stoloff, N. Physical and mechanical metallurgy of Ni_3Al and its alloys. *Int. Mater. Rev.* **34**, 153–184 (1989).
5. Russell, A. M. Ductility in intermetallic compounds. *Adv. Eng. Mater.* **5**, 629–639 (2003).
6. Sun, J., Pei, Y., Li, S., Zhang, H. & Gong, S. Improvement in ductility of high strength polycrystalline Ni-rich Ni_3Al alloy produced by EB-PVD. *J. Alloy. Compd.* **614**, 196–202 (2014).
7. Song, T. et al. Strong and ductile titanium–oxygen–iron alloys by additive manufacturing. *Nature* **618**, 63–68 (2023).
8. Smith, T. M. et al. A 3D printable alloy designed for extreme environments. *Nature* **617**, 513–518 (2023).
9. Liu, M. et al. Laser powder bed fusion of a Ni_3Al -based intermetallic alloy with tailored microstructure and superior mechanical performance. *Adv. Powder Mater.* **3**, 100152 (2024).
10. Chai, H. et al. Microstructure and cracking behavior of Ni_3Al -based IC21 alloy fabricated by selective laser melting. *Mater. Charact.* **196**, 112592 (2023).
11. Khomutov, M. et al. Effect of hot isostatic pressing on structure and properties of intermetallic NiAl–Cr–Mo alloy produced by selective laser melting. *Intermetallics* **120**, 106766 (2020).
12. Shi, X. et al. The crack and pore formation mechanism of Ti–47Al–2Cr–2Nb alloy fabricated by selective laser melting. *Int. J. Refract. Met. Hard Mater.* **91**, 105247 (2020).
13. Zhang, M. et al. Microstructure and mechanical properties of twin wire and arc additive manufactured Ni_3Al -based alloy. *J. Mater. Process. Technol.* **303**, 117529 (2022).
14. Yao, Y., Xing, C., Peng, H., Guo, H. & Chen, B. Solidification microstructure and tensile deformation mechanisms of selective electron beam melted Ni_3Al -based alloy at room and elevated temperatures. *Mater. Sci. Eng., A* **802**, 140629 (2021).
15. Shen, C., Pan, Z., Ma, Y., Cui, D. & Li, H. Fabrication of iron-rich Fe–Al intermetallics using the wire-arc additive manufacturing process. *Addit. Manuf.* **7**, 20–26 (2015).
16. Qua, H., Li, P., Zhang, S., Li, A. & Wang, H. The effects of heat treatment on the microstructure and mechanical property of laser melting deposition γ -TiAl intermetallic alloys. *Mater. Des.* **31**, 2201–2210 (2010).
17. Wang, L. et al. Fabrication of γ -TiAl intermetallic alloy using the twin-wire plasma arc additive manufacturing process: Microstructure evolution and mechanical properties. *Mater. Sci. Eng., A* **812**, 141056 (2021).
18. Yue, H. et al. Effect of heat treatment on the microstructure and anisotropy of tensile properties of TiAl alloy produced via selective electron beam melting. *Mater. Sci. Eng., A* **803**, 140473 (2021).
19. Zhou, Y. et al. Effect of heat treatments on the microstructure and mechanical properties of Ti_2AlNb intermetallic fabricated by selective laser melting. *Mater. Sci. Eng., A* **817**, 141352 (2021).
20. Zhang, Z., Zhou, Y., Zhou, S., Zhang, L. & Yan, M. Mechanically blended Al: simple but effective approach to improving mechanical property and thermal stability of selective laser-melted Inconel 718. *Metall. Mater. Trans. A* **50**, 3922–3936 (2019).
21. Wang, H. et al. Selective laser melting of the hard-to-weld IN738LC superalloy: Efforts to mitigate defects and the resultant microstructural and mechanical properties. *J. Alloy. Compd.* **807**, 151662 (2019).

22. Wang, X., Carter, L. N., Pang, B., Attallah, M. M. & Loretto, M. H. Microstructure and yield strength of SLM-fabricated CM247LC Ni-Superalloy. *Acta Mater.* **128**, 87–95 (2017).
23. Kürnstener, P. et al. High-strength Damascus steel by additive manufacturing. *Nature* **582**, 515–519 (2020).
24. Zhang, D. et al. Additive manufacturing of ultrafine-grained high-strength titanium alloys. *Nature* **576**, 91–95 (2019).
25. Zhu, Y. et al. Ultrastrong nanotwinned titanium alloys through additive manufacturing. *Nat. Mater.* **21**, 1258–1262 (2022).
26. Zhang, T. et al. In situ design of advanced titanium alloy with concentration modulations by additive manufacturing. *Science* **374**, 478–482 (2021).
27. Lin, D. et al. Effects of annealing on the structure and mechanical properties of FeCoCrNi high-entropy alloy fabricated via selective laser melting. *Addit. Manuf.* **32**, 101058 (2020).
28. Brif, Y., Thomas, M. & Todd, I. The use of high-entropy alloys in additive manufacturing. *Scr. Mater.* **99**, 93–96 (2015).
29. Nguyen, T., Huang, M., Li, H., Tran, V. & Yang, S. Microstructure and tensile properties of duplex phase $Al_{0.25}FeMnNiCrCu_{0.5}$ high entropy alloy fabricated by laser melting deposition. *J. Alloy. Compd.* **871**, 159521 (2021).
30. Ren, J. et al. Strong yet ductile nanolamellar high-entropy alloys by additive manufacturing. *Nature* **608**, 62–68 (2022).
31. Yao, N. et al. Ultrastrong and ductile additively manufactured precipitation-hardening medium-entropy alloy at ambient and cryogenic temperatures. *Acta Mater.* **236**, 118142 (2022).
32. Lin, W.-C. et al. Microstructure and tensile property of a precipitation strengthened high entropy alloy processed by selective laser melting and post heat treatment. *Addit. Manuf.* **36**, 101601 (2020).
33. Chen, P., Yang, C., Li, S., Attallah, M. M. & Yan, M. In-situ alloyed, oxide-dispersion-strengthened CoCrFeMnNi high entropy alloy fabricated via laser powder bed fusion. *Mater. Des.* **194**, 108966 (2020).
34. Zhou, R., Liu, Y., Liu, B., Li, J. & Fang, Q. Precipitation behavior of selective laser melted FeCoCrNiCo_{0.05} high entropy alloy. *Intermetallics* **106**, 20–25 (2019).
35. Li, B. et al. Selective laser melting of CoCrFeNiMn high entropy alloy powder modified with nano-TiN particles for additive manufacturing and strength enhancement: Process, particle behavior and effects. *Powder Technol.* **360**, 509–521 (2020).
36. Knowles, D., Thomas, C., Keen, D. & Chen, Q. In service embrittlement of cast 20Cr32Ni1Nb components used in steam reformer applications. *Int. J. Press. Vessels Pip.* **81**, 499–506 (2004).
37. Baker, I. & Munroe, P. Improving intermetallic ductility and toughness. *JOM* **40**, 28–31 (1988).
38. Chookajorn, T., Murdoch, H. A. & Schuh, C. A. Design of stable nanocrystalline alloys. *Science* **337**, 951–954 (2012).
39. Takasugi, T., George, E., Pope, D. & Izumi, O. Intergranular fracture and grain boundary chemistry of Ni₃Al and Ni₃Si. *Scr. Metall.* **19**, 551–556 (1985).
40. Chiba, A., Hanada, S. & Watanabe, S. Correlation between ductility and ordering energy of Ni₃Al. *Mater. Trans., JIM* **31**, 824–827 (1990).
41. Gazda, A., Rothova, V. & Cermak, J. Interdiffusion in pseudobinary sections of Ni₃Al–Co ternary system. *Intermetallics* **10**, 859–864 (2002).
42. Zhao, S. & Osetsky, Y. Structural and chemical disorder enhance point defect diffusion and atomic transport in Ni₃Al-based γ' phase. *Acta Mater.* **207**, 116704 (2021).
43. Liu, C. T., White, C. & Horton, J. Effect of boron on grain-boundaries in Ni₃Al. *Acta Metall.* **33**, 213–229 (1985).
44. Lee, T., Robertson, I. & Birnbaum, H. Interaction of dislocations with grain boundaries in Ni₃Al. *Acta Metall.* **40**, 2569–2579 (1992).
45. Yang, T. et al. Multicomponent intermetallic nanoparticles and superb mechanical behaviors of complex alloys. *Science* **362**, 933–937 (2018).
46. Zhang, M. et al. Tensile strength prediction of dual-phase Al_{0.6}CoCrFeNi high-entropy alloys. *Int. J. Miner., Metall. Mater.* **27**, 1341–1346 (2020).
47. Lin, Y., Yang, H. & Li, L. Effects of solutionizing cooling processing on γ' (Ni₃Nb) phase and work hardening characteristics of a Ni-Fe-Cr-base superalloy. *Vacuum* **144**, 86–93 (2017).
48. Hao, D. et al. Formability of TRIP/TWIP steel containing manganese of 18.8%. *J. Iron Steel Res., Int.* **18**, 36–40 (2011).
49. Qian, L. et al. Enhancing both strength and ductility of low-alloy transformation-induced plasticity steel via hierarchical lamellar structure. *Scr. Mater.* **183**, 96–101 (2020).
50. Viguier, B. Dislocation densities and strain hardening rate in some intermetallic compounds. *Mater. Sci. Eng., A* **349**, 132–135 (2003).
51. Osmundsen, R. & Baker, I. The annihilation of antiphase boundary tubes and their effect on strengthening in Ni₃Al. *Acta Mater.* **237**, 118185 (2022).
52. Li, X., Lu, L., Li, J., Zhang, X. & Gao, H. Mechanical properties and deformation mechanisms of gradient nanostructured metals and alloys. *Nat. Rev. Mater.* **5**, 706–723 (2020).
53. Li, J., Zhang, Q., Huang, R., Li, X. & Gao, H. Towards understanding the structure–property relationships of heterogeneous-structured materials. *Scr. Mater.* **186**, 304–311 (2020).
54. Jiang, J., Chen, Z., Ma, H., Xing, H. & Li, X. Strength-ductility synergy in heterogeneous-structured metals and alloys. *Matter* **5**, 2430–2433 (2022).
55. Paidar, V., Pope, D. & Yamaguchi, M. Structural stability and deformation behavior of L1₂ ordered alloys. *Scr. Metall.* **15**, 1029–1031 (1981).
56. Gong, X. et al. Alloying effects on site preference, mechanical properties, and deformation behavior of L1₂ Co–Ti-based alloys. *J. Mater. Res. Technol.* **24**, 1429–1441 (2023).
57. Okamoto, N. L., Takemoto, S., Chen, Z. M., Yamaguchi, M. & Inui, H. FCC metal-like deformation behaviour of Ir₃Nb with the L1₂ structure. *Int. J. Plasticity* **97**, 145–158 (2017).
58. Vamsi, K. & Karthikeyan, S. Deformation modes and yield strength anomaly in L1₂ compounds. *J. Alloy. Compd.* **860**, 158411 (2021).
59. Ungár, T., Ott, S., Sanders, P., Borbély, A. & Weertman, J. Dislocations, grain size and planar faults in nanostructured copper determined by high resolution X-ray diffraction and a new procedure of peak profile analysis. *Acta Mater.* **46**, 3693–3699 (1998).
60. Zhou, Y. et al. Highly printable, strong, and ductile ordered intermetallic alloy Figshare <https://doi.org/10.6084/m9.figshare.27988349> (2025).

Acknowledgements

T. Y. acknowledges the financial supports from the National Natural Science Foundation of China [Grant No. 52222112, 52101151], the Hong Kong Research Grant Council (RGC) [Grant No. 11208823]. Y.L.Z. acknowledges the financial supports from the National Natural Science Foundation of China [Grant No. 52101135], and Shenzhen Science and Technology Program [Grant No. JCYJ20220531095217039]. X.D.H. acknowledges the financial support from National Key R&D Program of China [Grant No. 2021YFA1200201]. M.Y. acknowledges the financial support from the Open Research Fund of Songshan Lake Materials Laboratory [Grant No.2021SLABFN18], and Shenzhen Science and Commission [Grant No. JCYJ2022081800612027]. The authors acknowledge the assistance of SUSTech Core Research Facilities. Atom probe tomography research was conducted at the Inter-University 3D Atom Probe Tomography Unit of City University of Hong Kong, which is supported by the CityU grant 9360161.

Author contributions

Y.H.Z., W.C.X., Y.L.Z., and T.Y. generated the idea and designed the experiments. Y.L.Z. and T.Y. supervised the research. Y.H.Z., D.W.W., and W.P.L. printed the samples and optimized the LPBF parameters. X.T. and

R.P.S. conducted the simulation of LPBF process. Z.L.S. and Z.B.A. performed the AC-STEM experiments. J.Z. and S.J.Z. conducted the DFT calculations. J.H.L. prepared the APT tips and collected and analyzed the APT data. Y.H.Z. drafted the initial manuscript. Y.L.Z, M.Y., X.D.H., C.T.L., and T.Y. discussed the results and revised the manuscript.

Competing interests

The authors declare no competing interests.

Additional information

Supplementary information The online version contains supplementary material available at <https://doi.org/10.1038/s41467-025-56355-2>.

Correspondence and requests for materials should be addressed to Yilu Zhao or Tao Yang.

Peer review information *Nature Communications* thanks Chaoyue Chen, Aijun Huang, Xiaoyan Li, Timothy Smith and the other, anonymous, reviewer(s) for their contribution to the peer review of this work. A peer review file is available.

Reprints and permissions information is available at <http://www.nature.com/reprints>

Publisher's note Springer Nature remains neutral with regard to jurisdictional claims in published maps and institutional affiliations.

Open Access This article is licensed under a Creative Commons Attribution-NonCommercial-NoDerivatives 4.0 International License, which permits any non-commercial use, sharing, distribution and reproduction in any medium or format, as long as you give appropriate credit to the original author(s) and the source, provide a link to the Creative Commons licence, and indicate if you modified the licensed material. You do not have permission under this licence to share adapted material derived from this article or parts of it. The images or other third party material in this article are included in the article's Creative Commons licence, unless indicated otherwise in a credit line to the material. If material is not included in the article's Creative Commons licence and your intended use is not permitted by statutory regulation or exceeds the permitted use, you will need to obtain permission directly from the copyright holder. To view a copy of this licence, visit <http://creativecommons.org/licenses/by-nc-nd/4.0/>.

© The Author(s) 2025